Journal of Solid State Chemistry **159,** 94–102 (2001)
doi:10.1006/jssc.2001.9136, available online at http://www.idealibrary.com on IDEAL®

Preparation and Characterization of Open Tunnel Oxide α-MnO_2 Precipitated by Ozone Oxidation

Norihito Kijima,[1] Hiroyuki Yasuda, Toshio Sato, and Yuji Yoshimura

National Institute of Materials and Chemical Research, 1-1 Higashi, Tsukuba, Ibaraki 305-8565, Japan

Received October 13, 2000; revised February 14, 2001; accepted March 5, 2001; published online May 4, 2001

Open tunnel oxide, α-MnO_2, without any large stabilizing cation has been successfully synthesized by ozone-oxidation of Mn^{2+} in H_2SO_4. Three kinds of acid (H_2SO_4, HNO_3, and HCl) and a wide variety of their concentrations and ozone-oxidation temperatures were tested to produce a well-crystallized α-MnO_2 specimen. The ozone-oxidation of Mn^{2+} in H_2SO_4 alone provided α-MnO_2 phase, while γ-MnO_2 phases were always formed in HNO_3 or HCl. High reaction temperatures (> 70°C) and high concentrations of H_2SO_4 (> 2 *M*) were necessary for the α-MnO_2 formation. X-ray and electron diffraction patterns confirmed that α-MnO_2 has the hollandite-type structure with space group of *I*4/*m* (No. 87) and lattice constants of $a = 9.78$ and $c = 2.85$ Å. Scanning and transmission electron microscopy images revealed a needle-like morphology for the α-MnO_2 crystals; the electron diffraction pattern verified the rod axis of the needle-like crystals in coincident with the direction of the tunnels. The nitrogen adsorption isotherm of α-MnO_2 exhibited the character of a typical Type IV, according to the IUPAC classification. The chemical, thermogravimetric, and temperature-programmed-desorption analyses indicated that H_2O molecules are occluded within the tunnel of α-MnO_2. Although N_2 molecules cannot penetrate the tunnel cavity, H_2O molecules can be trapped in the narrow tunnels with strong adsorption potential. © 2001 Academic Press

Key Words: **α-MnO_2; hollandite-type structure; precipitation using ozone oxidation; X-ray diffraction; electron diffraction; electron microscopy; crystal morphology; nitrogen adsorption isotherm; ultramicropore; mesopore; residual H_2O in tunnels.**

INTRODUCTION

Aluminosilicates including zeolites, clay minerals, and mesoporus silicates are well-known families of porous crystals. Recently, much attention has been focused on the porous materials of transition metal oxides. Several manganese oxides with tunnel structures have been extensively synthesized. Some detailed reviews on the manganese oxides with tunnel structures are provided by some researchers (1–5).

α-MnO_2 has the hollandite-type structure with space group of *I*4/*m* (No. 87), as shown in Fig. 1. It is known that α-MnO_2 alone has a tunnel structure without any large stabilizing cation in its tunnel cavity, whereas the other porous manganese oxides (e.g., romanechite and todorokite) have some large stabilizing cations in their tunnels (1–5). This open tunnel oxide, α-MnO_2, is an attractive material due to specific properties for various industrial applications (6–16), and there is fundamental interest for it as host material as a superionic conductor (17). Recently, α-MnO_2 has been intensively examined as an electrode material for lithium batteries (2, 6–11), as an ion-sieve and a molecular-sieve (4, 12–14), and as a catalyst (3, 4, 15, 16).

Many different synthetic techniques have been employed in the production of the α-MnO_2 phase. Many years ago, Brenet *et al*., reported that α-MnO_2 phase could be prepared by acid treatment of Mn_2O_3 in the absence of any foreign stabilizing cation (18); subsequently, he reported that the type and concentration of acid played an important role in determining the structure of the final product (19). In the early 1990s, Rossouw *et al*. synthesized α-MnO_2 phase by sulfuric acid treatment of Li_2MnO_3 (7). They have reported that the amount of residual Li content in the resulting material was 0.027 wt%; H_2O molecules (or H_3O^+ ions) partially occupy the tunnel of α-MnO_2 under air atmosphere. More recently, Muraoka *et al*. have reported that α-MnO_2 was prepared by starting from the hollandite-type $(NH_4)_xMn_8O_{16}$ and heating to remove ammonium ions from its structure (20). They have indicated the presence of nitrogen other than ammonium ions in the resulting material, and that this nitrogen had a strong chemical interaction with the hollandite structure.

The synthetic techniques have significant influence on the resultant properties. Much effort has been made to synthesize the open tunnel oxide, α-MnO_2. It is, however, difficult to synthesize a high purity and well-crystallized α-MnO_2 specimen because of residues of precursors. Therefore, we

[1] To whom correspondence should be addressed.

0022-4596/01 $35.00

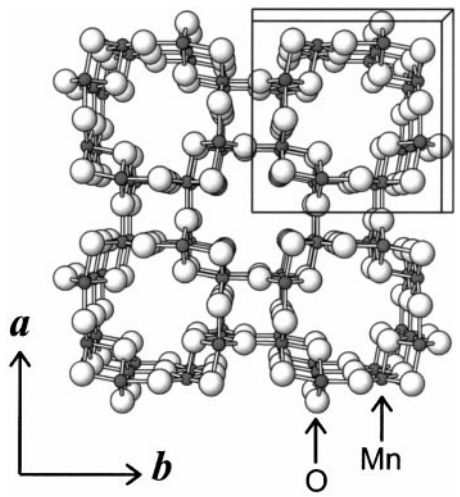

FIG. 1. Schematic drawing of the crystal structure of α-MnO_2 of a hollandite-type structure with space group of $I4/m$ (No. 87). The crystal structure is viewed down the c unit-cell axis; solid box indicates the unit cell.

focus on a redox precipitation method using ozone-oxidation. In this synthetic method, α-MnO_2 formation can proceed directly in solution without any metal ion other than Mn^{2+}.

Figure 2 shows a potential–pH equilibrium diagram for the Mn–H_2O system at 298.15 K and $[Mn^{2+}] = 0.1$ mol/l. Figure 2 was calculated by the thermodynamic database software FACT (CRCT, Ecole Polytechnique, Montreal, Quebec, Canada); this diagram is similar to that given by Pourbaix (21). Although MnO_2 is known to exit a wide variety of crystal structure forms, e.g., α-MnO_2, β-MnO_2 (1, 2, 4, 5, 22), ramsdellite-MnO_2 (1, 2, 4, 5, 22), γ-MnO_2 (1), ε-MnO_2 (1), δ-MnO_2 (1, 4, 5), and λ-MnO_2 (23), the crystal structure of MnO_2 is not specified in Fig. 2 because of the lack of thermodynamic data.

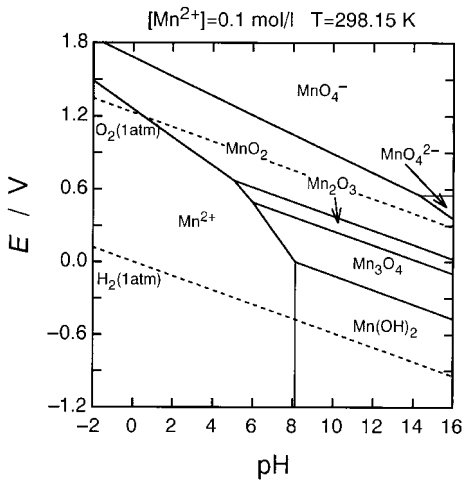

FIG. 2. Potential–pH equilibrium diagram for the Mn–H_2O system at 298.15 K and $[Mn^{2+}] = 0.1$ mol/l. Dotted lines show the equilibrium potentials for oxygen and hydrogen evolution reactions.

According to Fig. 2, the MnO_2 phase can be precipitated at lower pH and higher redox potential region; this high redox potential can be obtained by bubbling of ozone gas into the precipitation vessel. In an early work, Nishimura *et al.*, demonstrated that α-MnO_2, γ-MnO_2, or their mixture could be precipitated by ozone-oxidation of Mn^{2+} in H_2SO_4 (24, 25). In their works, other polymorphs of MnO_2 (e.g., β-MnO_2, ramsdellite-MnO_2) were not precipitated in H_2SO_4; ozone-oxidations of Mn^{2+} in other acids (e.g., HNO_3 and HCl) were not tested.

The initial purpose of this work is to prepare and characterize a well-crystallized specimen of α-MnO_2 without any large stabilizing cation in its tunnel. In this work, a high purity and well-crystallized α-MnO_2 specimen has been elaborated by the redox precipitation method using ozone-oxidation and characterized by powder X-ray diffraction, electron diffraction, electron microscopy, nitrogen adsorption isotherm, chemical analysis, thermogravimetric analysis, and temperature-programmed-desorption analysis.

Furthermore, we extensively investigated the effects of several acids (H_2SO_4, HNO_3, and HCl), their concentrations, and reaction temperatures in the ozone-oxidation of Mn^{2+} for the first time. Our experimental results verified that the ozone-oxidation of Mn^{2+} in H_2SO_4 alone provided α-MnO_2 phase, while γ-MnO_2 phases were always formed in HNO_3 or HCl. Moreover, other polymorphs of MnO_2 (e.g., β-MnO_2 and ramsdellite-MnO_2) were not obtained by the ozone-oxidation of Mn^{2+} in H_2SO_4, HNO_3, or HCl. Presently, the formation mechanism of α-MnO_2 has not yet been elucidated at the molecular level. It is our hope that the results presented below will be fruitful and helpful to verify and clarify the formation mechanism of the hollandite structure.

EXPERIMENTAL

Sample Preparation

α-MnO_2 was elaborated by the precipitation method using ozone-oxidation. Figure 3 illustrates the experimental apparatus for precipitation synthesis using ozone. A wide variety of ozone-oxidation temperature and concentration of solution were tested as part of our effort to produce a well-crystallized α-MnO_2. Furthermore, to study the influence of anions during the α-MnO_2 formation, three pairs of manganese-salt-hydrate and acid ($MnSO_4 \cdot 5H_2O$ and H_2SO_4, $Mn(NO_3)_2 \cdot 6H_2O$ and HNO_3, $MnCl_2 \cdot 4H_2O$ and HCl) were used in preparing the solution containing Mn^{2+}. The choice of acid, its concentration, and its reaction temperature were important in order to obtain α-MnO_2. The sample preparation conditions are described below in Results and Discussion.

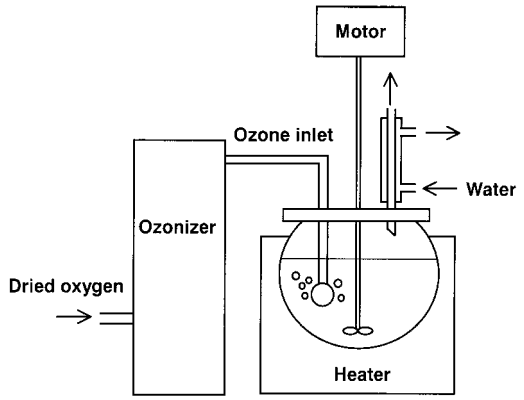

FIG. 3. Schematic illustration of the experimental apparatus of precipitation synthesis using ozone.

The typical synthesis procedure to produce a well-crystallized α-MnO_2 is as follows. Fourteen grams of $MnSO_4 \cdot 5H_2O$ (99.9%, Wako Pure Chemical Ind., Ltd.) was dissolved in 600 ml of 3 *M* H_2SO_4; subsequently, this solution was heated up to 80°C with stirring at 200 rpm. After reaching 80°C, the solution was bubbled by O_3 gas that was partially transformed from dried O_2 gas by an ozonizer (Nippon Ozone Co., Ltd., QOT-31R-2). The flowing rate of mixture of O_3 and O_2 was 40 cm^3/min; the concentration of O_3 was 135 l^3. When the O_3 gas was introduced into the reactor, the solution rapidly changed from colorless to pale pink and then precipitation occurred gradually. After ozone bubbling was carried out for 3 h, the resultant product was filtered and washed with distilled water until the washings were free from H_2SO_4. It was then freeze-dried in evacuated bottles for about 10 h using a freeze-dryer (Yamato Scientific Co., Ltd., DC-55A).

Characterization

Hydrogen content in the precipitated product was determined by combustion analysis using an elemental analyzer (CE Instruments EA1110). Manganese content in the product dissolved in HCl was evaluated by inductively coupled plasma-atomic emission spectroscopy (ICP-AES) with a Thermo Jarrell-Ash Co. IRIS/AP. Oxygen content in the product was determined from the results of the following titration method and the H/Mn mole ratio estimated by the above elemental analyses. The sample (about 0.1 g) was dissolved into an excess of 10 ml $H_2C_2O_4$ (0.5 mol/l) and 10 ml H_2SO_4 (0.5 mol/l) to reduce all the Mn^{n+} to Mn^{2+}. The excess $C_2O_4^{2-}$ in the solution was determined by titration at around 60°C with a standard solution of $KMnO_4$ (0.02 mol/l, Wako Pure Chemical Ind., Ltd.).

The crystal structure of the products was analyzed by powder X-ray diffraction (XRD) using a MAC science MAC-MXP^{18} diffractometer with Cu$K\alpha$ monochromatic radiation. Lattice constants were determined by extrapolation to Bragg angle $2\theta = 180°$, using extrapolation function $\cos^2\theta/\sin\theta$.

The morphology of the products was examined in a TOPCON DS-720 scanning electron microscope (SEM), equipped with a field emission gun, at 13 kV. A powder specimen was located on the mounted carbon tape and then spattered with about 10 nm-thick Au–Pd to suppress charging during the measurement.

The microstructure of the products was studied by transmission electron microscopy (TEM) with a HITACH HF-2000 microscope, operating at an acceleration voltage of 200 kV. The electron diffraction (ED) patterns were also measured by the electron microscope. Lattice constants were estimated by the relation $L\lambda = rd$, where L is the camera length, λ is the radiation, r is the distance between diffraction spots on film, and d is the lattice-plane spacing. The ED patterns were obtained from the various particles and d-spacings were measured, to an accuracy of $\pm$ 0.1 Å, using the ED pattern of Au as a reference standard.

The surface area and pore structure of the product were examined by nitrogen adsorption isotherm at 77 K using a BEL Japan BELSORP-28SA. A powder specimen was outgassed at 300°C for 1 h under 10^{-3} Torr before the measurement.

The content and characteristics of water in the product were studied by thermogravimetric (TG) and temperature-programmed-desorption (TPD) analyses. A well-crushed and sieved powder specimen was used for both analyses. These measurements were carried out from 25 to 1000°C at a linear heating rate of 5°C/min in flowing of mixture of O_2 (50 cm^3/min) and N_2 (200 cm^3/min). The TG curve was obtained using a MAC science TG-DTA 2000. The TPD analysis was performed using a quadruple mass spectrometer (ANELVA M-QA200TS); the amount of desorbed H_2O was calculated on the basis of the peak area of mass number 18.

RESULTS AND DISCUSSION

Sample Preparation of α-MnO_2

Figure 4 shows the relation between the crystal structure of precipitated products and the synthesis conditions (the initial concentration of acids and the ozone-oxidation temperature). As seen in Fig. 4, the crystal structure of precipitated products evidently depended on the kind of acid, its concentration, and the ozone-oxidation temperature.

Figure 4a plots the results of ozone-oxidation of $MnSO_4$ dissolved in H_2SO_4. The α-MnO_2 phases were produced at high H_2SO_4 concentrations and high reaction temperatures. In contrast, γ-MnO_2 phases were obtained at lower H_2SO_4 concentrations and lower temperatures. This tendency is in good agreement with the result by Nishimura *et al.* (25). Higher concentrations of H_2SO_4 ($> 2\ M$) are

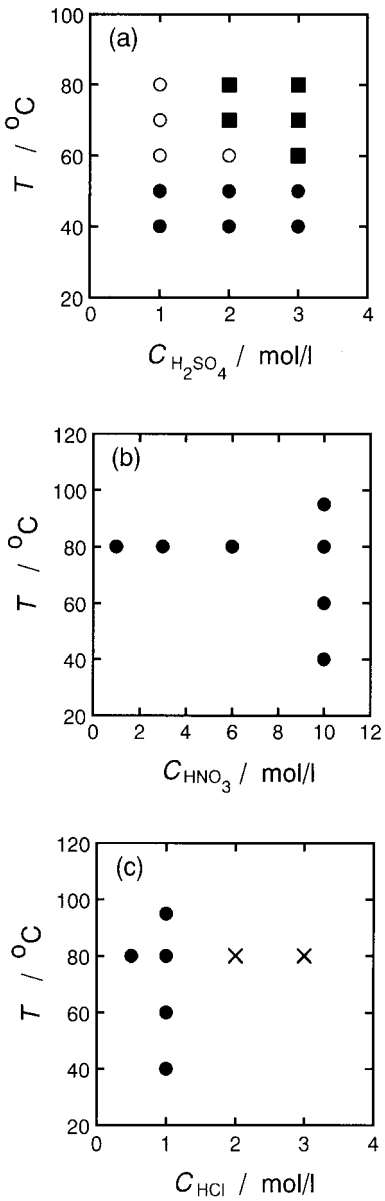

FIG. 4. Relation between the crystal structure of precipitated products and synthesis conditions (the initial concentration of acids and the ozone-oxidation temperature). Ozone-oxidations of Mn^{2+} are carried out in (a) H_2SO_4, (b) HNO_3, or (c) HCl at 40–95°C for 3 h; initial concentration of Mn^{2+} is 0.1 mol/l for each reaction: (■) α-MnO_2 phase; (●) γ-MnO_2 phase; (○) mixture of α-MnO_2 and γ-MnO_2 phases; (×) no precipitation within 3 h.

necessary for the α-MnO_2 formation than when using K^+, NH_4^+, or Rb^+ template (6).

Figure 5 presents the representative result of the powder X-ray diffraction patterns for the products precipitated by ozone-oxidation of $MnSO_4$ dissolved in 3 *M* H_2SO_4 at 40–80°C. It is obvious from Fig. 5 that a single phase of α-MnO_2 could be readily formed at the reaction temperatures of 60–80°C; the diffraction peaks of the α-MnO_2 product became stronger and shaper with increasing reaction temperature. All the diffraction peaks in Figs. 5a–5c were indexed of tetragonal symmetry with space group of $I4/m$ (No. 87). Lattice constants were estimated from Fig. 5a to be $a = 9.78$ and $c = 2.85$ Å, which are in good agreement with those reported on α-MnO_2 ($a = 9.78$ and $c = 2.86$ Å) prepared by treating Li_2MnO_3 with H_2SO_4 (7) and K^+-extracted α-MnO_2 ($a = 9.80$ and $c = 2.86$ Å) (8). At reaction temperatures below 50°C, a few broad diffraction peaks were observed, as shown in Figs. 5d and 5e. These patterns are similar to those of γ-MnO_2 reported by many workers (1, 8, 9, 24). The structure of γ-MnO_2 was described first as a random intergrowth of β-MnO_2 (rutile-type) and ramsdellite-MnO_2 layers (22, 26) and was then shown to incorporate microtwinning defects (1). In our experiments, the positions and profiles of diffraction peaks of the γ-MnO_2 products slightly changed depending on the preparation conditions.

In contrast to the ozone-oxidation of $MnSO_4$ dissolved in H_2SO_4, γ-MnO_2 phases were always formed by ozone-oxidations of $Mn(NO_3)_2$ dissolved in HNO_3 or $MnCl_2$ dissolved in HCl within our experimental conditions. As plotted in Fig. 4b, a single-phase of γ-MnO_2 was precipitated over reaction temperatures of 40–95°C and HNO_3 concentrations of 1–10 mol/l. In an earlier report (9), β-MnO_2 phase was formed by treating Mn_2O_3 with 9 *M* HNO_3 at 95°C. However, β-MnO_2 phase could not be produced by the ozone-oxidation of Mn^{2+} in 10 *M* HNO_3 at 95°C. As shown in Fig. 4c, a single-phase of γ-MnO_2 was also precipitated in HCl over the reaction temperatures of 40–95°C and HCl concentrations of 0.5–1 mol/l. When the concentration of HCl was beyond 1 mol/l, precipitation did not take place; manganese oxides can be dissolved in such high concentrated HCl.

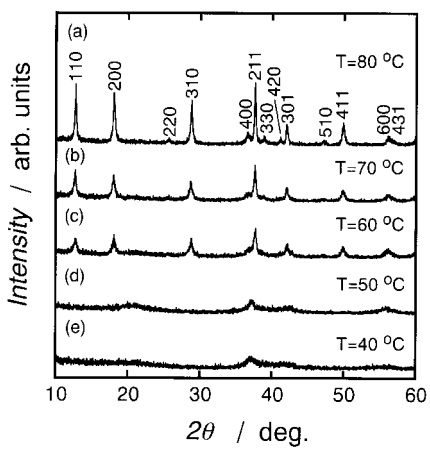

FIG. 5. Representative result of the powder X-ray diffraction patterns for the products precipitated by ozone-oxidation of $MnSO_4$ dissolved in 3 *M* H_2SO_4 for 3 h at (a) 80°C, (b) 70°C, (c) 60°C, (d) 50°C, and (e) 40°C, respectively.

Rossouw *et al.* reported the treatment of Mn_2O_3 with H_2SO_4, HCl, HNO_3, CH_3COOH, or H_3PO_4 at several acid concentrations and reaction temperatures (9). They have demonstrated that α-MnO_2 phase can be formed when a concentrated 4.5 *M* H_2SO_4 solution is used, and that the kinetics of the reaction is highly dependent on temperature. Furthermore, they have indicated that α-MnO_2 phase could not be synthesized by the reaction of Mn_2O_3 with any acid other than H_2SO_4. These tendencies correspond to our results of the ozone-oxidation of Mn^{2+} in H_2SO_4, HNO_3, or HCl, though a different synthesis method is used. The reactions proceeding in H_2SO_4 alone provide α-MnO_2 phase; a sufficiently high concentration of H_2SO_4 is necessary for α-MnO_2 formation.

The hollandite-type structure is constructed from double chains of $[MnO_6]$ octahedra forming (2×2) tunnels, as seen in Fig. 1; the rutile-type structure is composed of single chains of the octahedra (1, 2, 4, 5, 22). As far as we know, the formation mechanism of the hollandite structure has not been reported, although mechanisms of hydrothermal crystallization of the rutile-type TiO_2 have been proposed (27, 28). Formation process of the $[MnO_6]$ octahedron in the hollandite structure might be similar to that in the rutile structure. Moreover, some template instead of K^+, Ba^{2+}, or NH_4^+ would be needed to produce such large (2×2) tunnels during the α-MnO_2 formation in H_2SO_4. It is believed that sulfuric acid in aqueous solution produces the hydroxonium ion (29). The H_3O^+ might act as the template during the α-MnO_2 formation in H_2SO_4.

Crystal Morphology of α-MnO_2

Figure 6 shows SEM images of the precipitated α-MnO_2 and γ-MnO_2 products. As seen in Fig. 6a, the particle surface of precipitated α-MnO_2 was covered almost uniformly with needle-like crystals. The corresponding XRD pattern of this α-MnO_2 product is shown in Fig. 5a; highly asymmetric reflections due to anisotropic broadening are observed, which is consistent with the α-MnO_2 product having needle-like crystals. It is known that natural hollandite minerals are found typically as fibrous crystals and less commonly as prismatic crystals in hydrothermal vein deposits (5). Our result is consistent with this fact. In contrast to the α-MnO_2 product, γ-MnO_2 product exhibited nearly spherical grain morphology and smooth surface, as shown in Fig. 6b. This difference in crystal morphology between α-MnO_2 and γ-MnO_2 can be related to different formation mechanisms and reaction kinetics.

Figure 7 illustrates the ED pattern and shows a TEM image of the tip of the needle-like crystal of α-MnO_2. As shown in Fig. 7a, electron diffraction spots were not diffuse but fine; no satellite spots were detected. All of the diffraction spots have been indexed of tetragonal symmetry with space group of $I4/m$ (No. 87); lattice constants are estimated

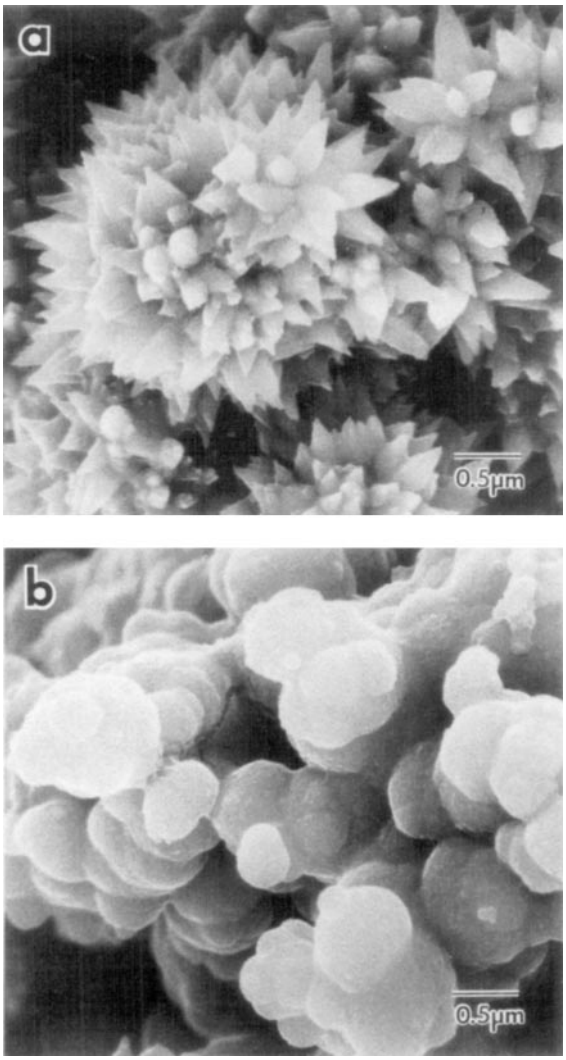

FIG. 6. SEM images of (a) α-MnO_2 and (b) γ-MnO_2 products. Both specimens are precipitated by ozone-oxidation of $MnSO_4$ dissolved in 3 *M* H_2SO_4 for 3 h at 80°C for α-MnO_2 and 40°C for γ-MnO_2, respectively.

to be $a = 9.8$ and $c = 2.8$ Å, which give excellent agreement with the cell dimension obtained from the powder X-ray diffraction analysis. As seen in Fig. 7b, the TEM image verifies that the tip of the needle-like crystal of α-MnO_2 consists mainly of domains of single crystal since the straight lattice arrangement is observed, whereas the surface is slightly covered with amorphous components. It is obvious from the ED pattern and the TEM image that these needle-like crystals are growing to the *c* axis of the unit cell, which is also the direction of the tunnel.

To investigate the crystal growth mechanism, the precipitated α-MnO_2 particles (shown in Fig. 6a) were kept at 3 *M* H_2SO_4 at 80°C for 7 days without ozone bubbling. Figure 8 shows SEM and TEM images of the α-MnO_2 crystals after aging without ozone-oxidation. The crystal morphology drastically transformed from ragged particles

(Fig. 6a) to rod-shaped crystals (Fig. 8). As seen in Fig. 8a, some rod-shaped crystals contain several single crystals aligned parallel in a column; ED patterns conformed the rod axis of the rod-shaped crystals in coincident with the *c* axis of the unit cell.

This morphological transformation reveals that rearrangements between Mn and O atoms progress at the particle surface of α-MnO_2 without ozone-oxidation. It is reported that the transformation without changing the manganese valence occurs in H_2SO_4 at 80°C according to the following reaction: $Li_2MnO_3 \rightarrow$ α-$MnO_2 + Li_2O$ (7). Therefore, it can be presumed that high concentration of H_2SO_4 and high reaction temperature play an important role in the crystal growth of α-MnO_2; the ozone-oxidation is mainly related to nucleation of MnO_2 particles.

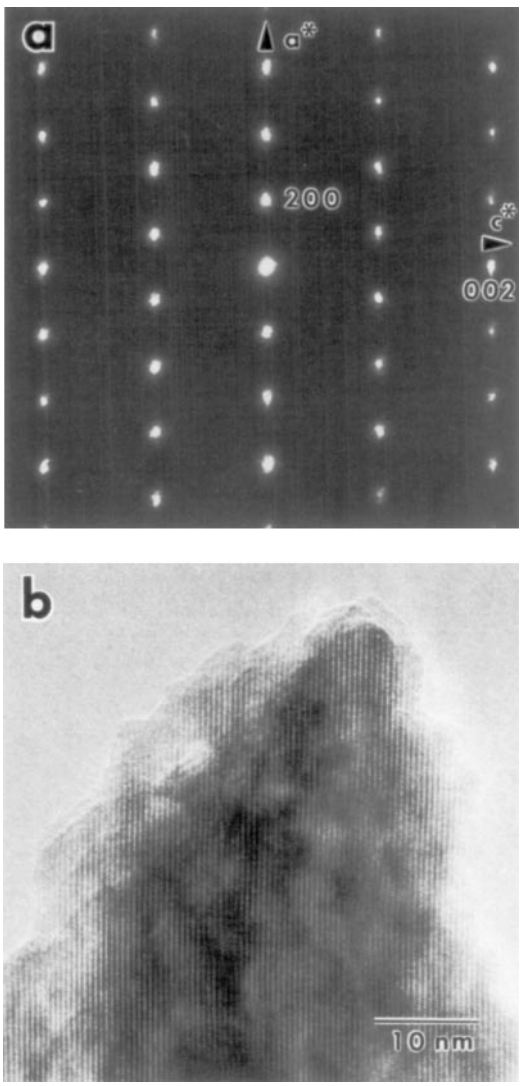

FIG. 7. (a) ED pattern and (b) TEM image of the tip of needle-like crystal of α-MnO_2. The incident electron beam is parallel to [010] direction. The specimen is precipitated by ozone-oxidation of $MnSO_4$ dissolved in 3 *M* H_2SO_4 at 80°C for 3 h.

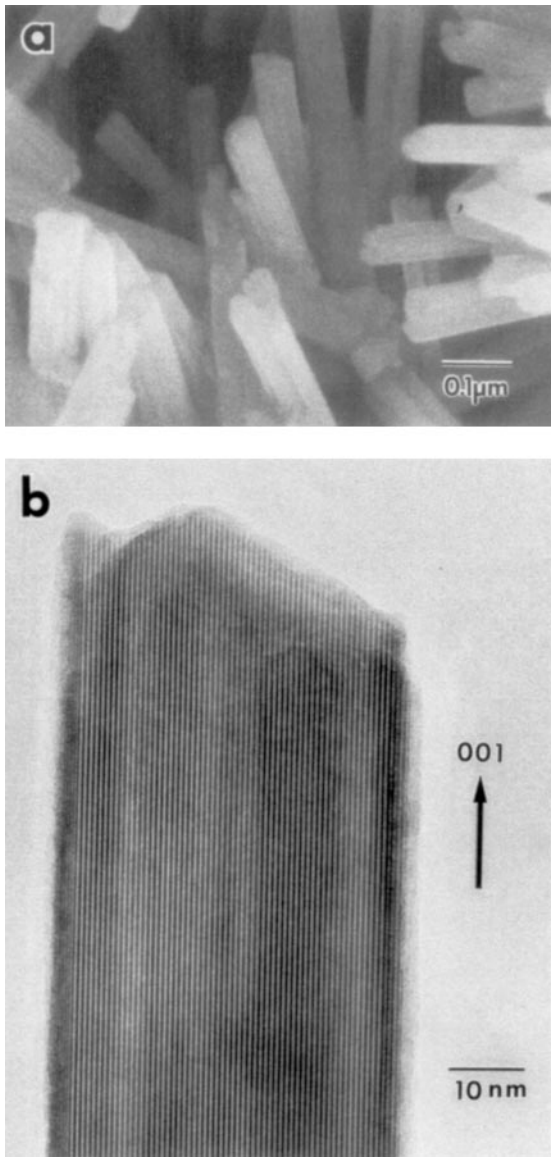

FIG. 8. (a) SEM and (b) TEM images of the rod-shaped crystals of α-MnO_2. The crystals are prepared by aging of the precipitated particles (Fig. 6a) in 3 *M* H_2SO_4 at 80°C for 7 days without ozone bubbling.

Pore Structure of α-MnO_2

Figure 9 depicts the nitrogen adsorption and desorption isotherm of α-MnO_2. The amount of adsorbed gas increased abruptly at the lower P/P_0 regions and then linearly increased with increasing the P/P_0. This initial dependency is attributed to the monolayer–multilayer adsorption. Subsequently, the hysteresis loop was observed at the middle range of $0.3 < P/P_0 < 0.9$, which is associated with capillary

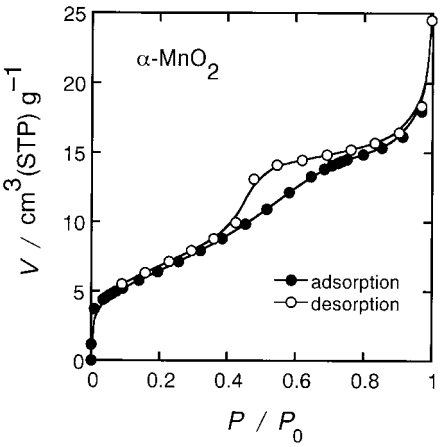

FIG. 9. Adsorption and desorption isotherms of nitrogen gas at 77 K on α-MnO_2. The quantities of adsorbed or desorbed nitrogen per mass of α-MnO_2 are expressed as the volume in STP (standard temperature and pressure); the nitrogen pressure P is normalized to the saturation pressure P_0.

condensation taking place in mesopores. Finally, the amount of adsorbed gas increased in the higher P/P_0 regions. According to the International Union of Pure and Applied Chemistry (IUPAC) (30), the nitrogen adsorption isotherm of the α-MnO_2 product exhibits the character of a typical Type IV.

The Brunauer–Emmett–Teller (BET) method (31) was applied to the surface area determination since the Type IV isotherm was observed. The linear portion of the BET plot was found to be in the $0.05 < P/P_0 < 0.3$ range, which is not given in the figure. The BET surface area, S_{BET}, was estimated to be 23.8 m^2/g; the BET constant, C_{BET}, was 72.3. For comparison, Langmuir surface area, $S_{Langmuir}$, was calculated using the data in the range of $0.01 < P/P_0 < 0.05$. The $S_{Langmuir}$ was estimated to be 20.2 m^2/g, which is in reasonable agreement with the S_{BET}.

As shown in Fig. 1, α-MnO_2 has a tunnel cavity in the crystal structure. To estimate the size of the tunnel cavity, electron density distribution maps in the α-MnO_2 structure were visualized from powder X-ray diffraction data by combining Rietveld analysis (32) and maximum entropy method (33). Recently, this analytical technique was applied to the estimation of electron density distribution in hydrated and dehydrated sodium-type zeolite LTA; the distribution of adsorbed water molecules in the cage was successfully visualized (34). From the electron density distribution map, the inner diameter of the tunnel cavity in the α-MnO_2 structure is estimated to be approximately 0.38 nm that is classified as ultramicropore (pore width < 0.7 nm) (35). This detailed result is going to be published elsewhere.

According to the adsorption study, empirical diameters of adsorbable molecules are reported to be 0.43 nm for N_2 at 77 K and 0.22 nm for H_2O at 25°C, respectively (36). The pore width in the α-MnO_2 structure (about 0.38 nm) is smaller than N_2 molecule size (0.43 nm) and larger than H_2O molecule size (0.22 nm). Furthermore, the nitrogen adsorption isotherm of α-MnO_2 is not Type I but Type IV. Indeed, initial rise due to micropore filling at the lower P/P_0 regions and plateau at the middle P/P_0 regions are not observed. Therefore, we can conclude that N_2 molecules cannot penetrate the tunnel cavity of α-MnO_2. More recently, N_2, O_2, H_2O, and NH_3 adsorption isotherms of α-MnO_2 were reported by Wang *et al.* (37). They reported that only H_2O and NH_3 molecules can be adsorbed in the tunnel cavity, which is consistent with our result.

The precipitated product of α-MnO_2 has not only ultramicropores (pore width < 0.7 nm) but also mesopores (pore width: $2 \sim 50$ nm) since the hysteresis loop due to capillary condensation is observed at the middle range of P/P_0. According to the IUPAC classification (30), the hysteresis loop in Fig. 9 is similar to the Type H2 loop. Many porous adsorbents (e.g., inorganic oxide gels and porous glasses) tend to give Type H2 loops, but the distribution of pore size and shape is not well defined in such systems; therefore, the Type H2 is especially difficult to interpret among several hysteresis loops (30). Since the Type H2 loop is observed, the mesopores in the α-MnO_2 product have no regular distribution of pore size and no specific pore shape. Origin of the mesopores is probably associated with a void in agglomerate composed of ragged particles (Fig. 6a).

Residual Water in the Tunnel of α-MnO_2

The general formula of α-MnO_2 is given as $A_{0-2}(Mn^{4+}, Mn^{3+})_8(O, OH)_{16}$, where A is a large cation, usually Ba^{2+} (hollandite) or K^+ (cryptomelane) (38). In our synthesized α-MnO_2 specimen, water molecules are accommodated at the A site normally occupied by the large cations.

The chemical composition of our synthesized α-MnO_2 product was determined to be $H_{0.48}MnO_{2.23}$ from the results of the titration and the elemental analyses. From this composition, the mean oxidation state of manganese was estimated to be $+3.98$, which is close to $+4$ within our experimental error. This result indicates that the valence of manganese in our specimen is mostly tetravalent; neutral H_2O molecules are dominant in the tunnels rather than H_3O^+ ions. Assuming that all manganese ions are tetravalent and ignoring the small amount of H^+, the amount of water in the product can be estimated to be 0.23 mol per mol of α-MnO_2.

Figure 10 shows the plot of a thermogravimetric (TG) analysis of the α-MnO_2 product. Result of the TG curve is in good agreement with those reported by many researchers (7, 12–14, 20). The first weight loss at around 25–400°C is attributed to the release of water; the subsequent mass loss at around 550°C corresponds to decomposition from α-MnO_2 to Mn_2O_3. From the TG analysis, the amount of

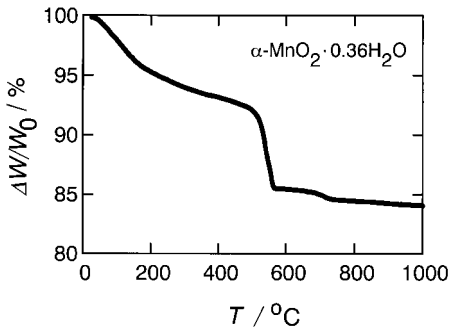

FIG. 10. Plot of the TG analysis of the α-$MnO_2 \cdot 0.36H_2O$ powder with a heating rate of 5°C/min in flowing mixture of O_2 (50 cm^3/min) and N_2 (200 cm^3/min). The specimen is prepared by ozone-oxidation of $MnSO_4$ dissolved in 3 *M* H_2SO_4 for 3 h at 80°C.

the release of water was estimated to be 0.36 mol per mol of α-MnO_2. This value is higher than that estimated by chemical analysis; this difference is mainly attributed to the idea that the following N_2 and O_2 gases were not well-dried. In summary, the thermal decomposition of the product is described in the reaction

$$\alpha\text{-}MnO_2 \cdot 0.36H_2O \xrightarrow{25^\circ C-400^\circ C} \alpha\text{-}MnO_2 + 0.36H_2O\uparrow$$

$$\xrightarrow{\sim 550^\circ C} \tfrac{1}{2}Mn_2O_3 + \tfrac{1}{4}O_2\uparrow. \qquad [1]$$

X-ray diffraction pattern of the heat-treated sample confirmed that the α-MnO_2 structure was retained up to at least 300°C without structural collapse; the α-MnO_2 dehydrated at 300°C has strong affinity for reabsorbing the water if exposed to air.

Figure 11 presents the profile of temperature-programmed desorption (TPD) of H_2O from the α-MnO_2 product. From the peak area over the 25–500°C range, the amount of desorbed H_2O was estimated to be about 0.3 mol per mol of α-MnO_2. This amount of desorbed H_2O is in reasonable agreement, within our experimental error, with those estimated by the chemical and TG analyses. As shown in Fig. 11, the desorption rate of H_2O increased rapidly with increasing temperature, reaching a maximum at 130°C; then it decreased granularly between 200 and 500°C. According to the result of H_2O-TPD for α-MnO_2 by Muraoka *et al.* (20), two desorption peaks at around 80 and 130°C are observed; Feng *et al.*, reported an endothermic peak at 80°C and a shoulder at 170°C in the differential-thermal-analysis (DTA) curve (13). Therefore, it can be presumed that two kinds of absorbed water with different chemical environments exist in the α-MnO_2 product.

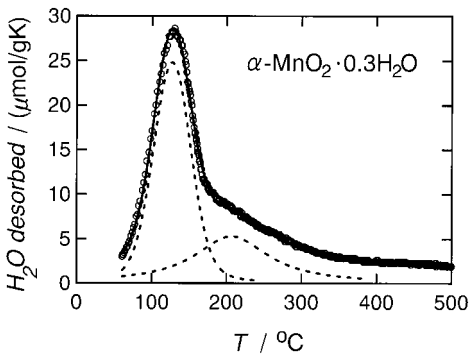

FIG. 11. Profile of the H_2O–TPD of the α-$MnO_2 \cdot 0.3H_2O$ powder with a heating rate of 5°C/min in flowing mixture of O_2 (50 cm^3/min) and N_2 (200 cm^3/min). The specimen is prepared by ozone-oxidation of $MnSO_4$ dissolved in 3 *M* H_2SO_4 for 3 h at 80°C. The two broken peaks indicate deconvoluted peaks; the fitted solid curve shows convolution of the two peaks.

To estimate the amounts of water adsorbed on different chemical states, we attempted to deconvolute the H_2O-TPD profile. This TPD profile can be empirically deconvoluted into two peaks; we simply assumed that each profile of desorption peak has the Voigt function (a convolution between Gaussian and Lorentzian), although most reported peak profiles are asymmetric due to readsorption depending on measurement condition. The two broken peaks in Fig. 11 indicate deconvoluted peaks; the fitted solid curve shows convolution of the two peaks. The peak temperatures of the first and second broken peaks are 127 and 207°C, respectively. These temperatures are slightly higher than those reported by Muraoka *et al.* (20), which might be attributed to experimental condition. The first peak at 127°C could be due to additional water associated with surface-adsorbed water; the gradual second peak at around 207°C would be attributed to additional water occluded within the tunnel of α-MnO_2. From the second peak area, the amount of H_2O desorbed from the tunnel was estimated to be about 0.1 mol per mol of α-MnO_2. This value is consistent with the amount of the large cations in the hollandite-type minerals (38).

The residual H_2O molecules in the tunnels appear to be disordered at room temperature since the waved background is observed on the XRD pattern of the α-MnO_2 product. Moreover, the H_2O molecules occluded within the tunnel can be removed from α-MnO_2 on heat treatment; therefore, the amount of H_2O in the tunnel could not be determined exactly by the chemical, TG, and H_2O-TPD analyses. Thus, it can be inferred that the H_2O molecules are trapped in the narrow tunnel with strong adsorption potential due to micropore filling, although the nature and locations of the residual H_2O molecules in the tunnel structure remain unclear at present. To verify and clarify the nature and locations of residual H_2O molecules in the tunnel structure, neutron diffraction investigation of deuterated α-MnO_2 specimen containing D_2O in its tunnel is in progress. A detailed structure study of α-$MnO_2 \cdot nD_2O$ is going to be published elsewhere.

SUMMARY

1. The ozone-oxidation of Mn^{2+} in H_2SO_4 provided α-MnO_2 phase, while γ-MnO_2 phases were always formed in HNO_3 or HCl. Other polymorphs of MnO_2 (e.g., β-MnO_2 and ramsdellite-MnO_2) could not be synthesized by the ozone-oxidation of Mn^{2+} in H_2SO_4, HNO_3, or HCl. High reaction temperatures ($> 70°C$) and high concentrations of H_2SO_4 ($> 2\ M$) were necessary for the α-MnO_2 formation.

2. SEM and TEM images revealed needle-like morphology for the α-MnO_2 crystals; ED pattern verified the rod axis of the α-MnO_2 crystals in coincident with the c axis of the unit cell. Rearrangements between Mn and O atoms proceeded at the surface of the α-MnO_2 crystals in $3\ M$ H_2SO_4 at 80°C without ozone-oxidation; the crystal morphology transformed from ragged particles to rod-shaped crystals.

3. The nitrogen adsorption isotherm of the α-MnO_2 product exhibited the character of a typical Type IV; the hysteresis loop was classified as Type H2, according to the IUPAC classification. The precipitated product of α-MnO_2 has not only ultramicropores but also mesopores.

4. The chemical, TG, and TPD analyses indicate that H_2O molecules are occluded within the tunnel of α-MnO_2. The H_2O molecules can be trapped in the narrow tunnel with strong adsorption potential due to micropore filling, although N_2 molecules cannot penetrate the tunnel cavity.

ACKNOWLEDGMENTS

We thank Dr. T. Ikeda (National Institute for Research in Inorganic Materials) for his valuable discussion. We are grateful to Dr. Y. Okada at the National Institute of Materials and Chemical Research (NIMC) for the FE-SEM measurements and Dr. T. Kuroiwa, also at NIMC, for the elemental analysis using ICP-AES.

REFERENCES

1. Y. Chabre and J. Pannetier, *Prog. Solid State Chem.* **23,** 1 (1995), and references therein.
2. M. M. Thackeray, *Prog. Solid State Chem.* **25,** 1 (1997), and references therein.
3. S. L. Brock, N. Duan, Z. R. Tian, O. Giraldo, H. Zhou, and S. L. Suib, *Chem. Mater.* **10,** 2619 (1998), and references therein.
4. Q. Feng, H. Kanoh, and K. Ooi, *J. Mater. Chem.* **9,** 319 (1999), and references therein.
5. J. E. Post, *Proc. Natl. Acad. Sci. U.S.A.* **96,** 3447 (1999), and references therein.
6. T. Ohzuku, M. Kitagawa, K. Sawai, and T. Hirai, *J. Electrochem. Soc.* **138,** 360 (1991).
7. M. H. Rossouw, D. C. Liles, and M. M. Thackeray, *Mater. Res. Bull.* **27,** 221 (1992).
8. Q. Feng, H. Kanoh, K. Ooi, M. Tani, and Y. Nakacho, *J. Electrochem. Soc.* **141,** L135 (1994).
9. M. H. Rossouw, D. C. Liles, and M. M. Thackeray, *Prog. Batteries Battery* **15,** 8 (1996).
10. C. S. Johnson, D. W. Dees, M. F. Mansuetto, M. M. Thackeray, D. R. Vissers, D. Argyriou, C.-K. Loong, and L. Christensen, *J. Power Sources* **68,** 570 (1997); C.S. Johnson, D. W. Dees, M. F. Mansuetto, M. M. Thackeray, D. R. Vissers, D. Argyriou, C.-K. Loong, and L. Christensen, *J. Power Sources* **75,** 183 (1998).
11. Y. Shao-Horn, S. A. Hackney, C. S. Johnson, and M. M. Thackeray, *J. Electrochem. Soc.* **145,** 582 (1998).
12. R. N. DeGuzman, Y.-F. Shen, E. J. Neth, S. L. Suib, C.-L. O'Young, S. Levine, and J. M. Newsam, *Chem. Mater.* **6,** 815 (1994).
13. Q. Feng, H. Kanoh, Y. Miyai, and K. Ooi, *Chem. Mater.* **7,** 148 (1995).
14. Y. Tanaka, M. Tsuji, and Y. Tamaura, *Phys. Chem. Chem. Phys.* **2,** 1473 (2000).
15. K. Sugiyama, H. Miura, Y. Nakano, H. Sekiwa, and T. Matsuda, *Bull. Chem. Soc. Jpn.* **59,** 2983 (1986).
16. S. Yamamoto, O. Matsuoka, I. Fukada, Y. Ashida, T. Honda, and N. Yamamoto, *J. Catal.* **159,** 401 (1996).
17. P. Strobel, J. Vicat, and D. T. Qui, *J. Solid State Chem.* **55,** 67 (1984).
18. J. Brenet and A. Grund, *C.R. Acad. Sci. Paris* **242,** 2343 (1956). [In French]
19. J. Brenet, *J. Power Sources* **39,** 349 (1992). [In French]
20. Y. Muraoka, H. Chiba, T. Atou, M. Kikuchi, K. Hiraga, Y. Syono, S. Sugiyama, S. Yamamoto, and J.-C. Grenier, *J. Solid State Chem.* **144,** 136 (1999).
21. M. Pourbaix, "Atlas of Electrochemical Equilibria in Aqueous Solutions," p. 286. Pergamon press, Oxford, 1966.
22. A. F. Wells, "Structural Inorganic Chemistry," 5th ed., p. 555. Oxford University Press, London, 1984.
23. J. C. Hunter, *J. Solid State Chem.* **39,** 142 (1981).
24. T. Nishimura and Y. Umetsu, *Shigen to Sozai* **107,** 805 (1991). [In Japanese]
25. T. Nishimura and Y. Umetsu, *Shigen to Sozai* **108,** 373 (1992). [In Japanese]
26. P. M. de Wolff, *Acta Crystallogr.* **12,** 341 (1959).
27. W.-J. Li, E.-W. Shi, and Z.-W. Yin, *J. Cryst. Growth* **208,** 456 (2000).
28. K. Yanagisawa and J. Ovenstone, *J. Phys. Chem. B* **103,** 7781 (1999).
29. P. Batamack and J. Fraissard, *Colloids Surf. A* **158,** 207 (1999).
30. K. S. W. Sing, D. H. Everett, R. A. W. Haul, L. Moscou, R. A. Pierotti, J. Rouquérol, and T. Siemieniewska, *Pure Appl. Chem.* **57,** 603 (1985).
31. S. J. Gregg and K. S. W. Sing, "Adsorption, Surface Area and Porosity," 2nd ed., p. 42. Academic Press, San Diego, 1982.
32. F. Izumi, "The Rietveld Method". (R. A. Young, Ed.), Chap. 13. Oxford University Press, Oxford, 1995; F. Izumi and T. Ikeda, *Mater. Sci. Forum* **321–324,** 1983 (2000).
33. S. Kumazawa, Y. Kubota, M. Takata, M. Sakata, and Y. Ishibasi, *J. Appl Crystallogr.* **26,** 453 (1993).
34. T. Ikeda, F. Izumi, T. Kodaira, and T. Kamiyama, *Chem. Mater.* **10,** 3996 (1998).
35. S. J. Gregg and K. S. W. Sing, "Adsorption, Surface Area and Porosity," 2nd ed., p. 244. Academic Press, San Diego, 1982.
36. H. Naono, M. Shimoda, N. Morita, M. Hakuman, K. Nakai, and S. Kondo, *Langmuir* **13,** 1297 (1997), and references therein.
37. Z.-M. Wang, S. Tezuka, and H. Kanoh, *Chem. Lett.* **2000,** 560 (2000).
38. J. E. Post, R. B. Von Dreele, and P. R. Buseck, *Acta Crystallogr. Sect. B: Struct. Sci.* **38,** 1056 (1982).